Microporous and Mesoporous Materials 330 (2022) 111618

Contents lists available at ScienceDirect

Microporous and Mesoporous Materials

journal homepage: www.elsevier.com/locate/micromeso

Mesoporous low silica X (MLSX) zeolite: Mesoporosity in loewenstein limit?

José María Gómez *, Ignacio Montes, Eduardo Díez, Araceli Rodríguez

Catálisis y Operaciones de Separación (CyPS), Department of Chemical and Materials Engineering. Faculty of Chemistry, Universidad Complutense de Madrid, 28040, Madrid, Spain

ARTICLE INFO

Keywords:
Mesoporous
LSX zeolite
Calcination
Oleic acid
Biojet fuel

ABSTRACT

Synthesis of Low Silica X zeolite (LSX) with hierarchical porosity was achieved. The low silicon/aluminum ratio of this zeolite allowed to increase the number of active sites, as cationic positions (>25%) respect to the previous mesoporous X zeolite. Mesoporosity was induced by using sodium dodecylbenzene sulfonate (SDBS) during the synthesis. A dissolution time of 24 h for SDBS improved the zeolite crystallinity, maintaining the FAU characteristic framework, with a silicon/aluminum molar ratio near the unity (<1.1), limit of the Lowenstein' rule. The surfactant removal at 773 K promoted the development of a wider pore size distribution. The heating rate highly determined the pore size distribution, resulting in a bimodal distribution (maxima at 80 Å and 290 Å) at low heating rate (1.3 K/min) and a unimodal distribution, with a maximum at 230 Å, at higher heating rate (8 K/min). The analysis by Transmission Electronic Microscopy (TEM) showed the mesoporous cavities in the zeolite nanoparticles. These cavities were generated by the SDBS spherical micelles removal. Mesoporous Low Silica X zeolite (MLSX) showed higher catalytic activity than the same zeolite without mesoporosity in the deoxygenation of oleic acid. The conversion reached a constant value around 100% with higher yield toward C_9–C_{18} hydrocarbons, representative fraction of sustainable aviation fuel (SAF). Therefore, this new mesoporous low silica X zeolite (MLSX) has a significant potential use as catalyst in the processing of bulky molecules.

1. Introduction

Zeolites are crystalline aluminosilicates, natural or synthetic, with a porous structure consisting of orderly distributed micropores in molecular dimensions. The structure is comprised of silicon and aluminum oxides tetrahedrons (TO^4) that coordinate using the oxygen atoms, as well as different extraframework cations (Na^+, K^+, Ca^{2+}, etc.) that compensate the negative charges produced by the aluminum tetrahedrons (AlO_4^-). They have been widely used as solid catalysts in petrochemical industries or as water treatment or gases purification and separation adsorbents. Even the zeolites have shown promising applications in biotechnology, in medicine, in renewable energy and environmental improvement or in sustainable fields, such as agriculture [1,2]. When using zeolites, there is an important trade off that must be considered. A high number of aluminum tetrahedrons increases the quantity of potential active sites and consequently the ion-exchange capacity. Although it puts in commitment the stability of the structure, since a zeolite will be more stable when the amount of silicon-oxides tetrahedrons increases [3].

Zeolites with a molar ratio of silicon/aluminum of 1.0 are usually referred to as Low Silica Zeolite X (LSX). This zeolite, respect to the aluminum content, is in the limit of the Löwenstein's rule which is generally accepted in zeolite synthesis. Löwenstein's rule implies that the Al–O–Al bond formation is forbidden in zeolites [4]. Therefore, the minimum silicon/aluminum molar ratio is 1.0. LSX zeolite presents a FAU-type structure, with a framework containing hexagonal prisms (double 6 rings) linked through sodalite cages. The final structure presents a 3-dimensional porous channel structure (7.4 Å) with supercages with 12 oxygen ring windows (≈13.0 Å). Usually, the synthesis of LSX zeolite is carried out according to the procedure described by Kühl [5] with some modifications, such as the use of microwave heating [6] or agricultural waste as silica source [7]. Even the synthesis of LSX zeolite/activated carbon [8] or of LSX/A zeolites [9] composites have been studied. Despite the fact it is the porous structure that gives zeolites their ability to be used in the different applications mentioned above, the limitations imposed by their pore size are important, such as steric hindrance to process bulky molecules, low diffusion rates due to the internal mass transfer resistance, deactivation by coking, etc. The induction of a hierarchical structure, containing both microporosity and meso/macroporosity, is emerging as a new and important method to

* Corresponding author.
E-mail address: segojmgm@ucm.es (J.M. Gómez).

https://doi.org/10.1016/j.micromeso.2021.111618
Received 26 July 2021; Received in revised form 30 November 2021; Accepted 2 December 2021
Available online 6 December 2021

improve their potential, overcoming their pore size limitations [10,11]. The hierarchical structure can be generated using different methods such as top-down and bottom-up methods. The first method is based on the modification of an already produced zeolite, for instance, dealumination, whilst the second one consists of synthesizing the zeolite with hierarchical structure by using a hard or soft template. Hard templates are those whose structure cannot be easily changed; meanwhile, soft template have the opposite definition [12,13]. The approach of synthesis using the latter has been an achievement fulfilled for zeolites with a high silicon/aluminum ratio, as well as different framework types such as MFI or Beta [14–16]. However, FAU structure is currently being studied by different methods to obtain the hierarchical structure [17–20].

The combination of both features in zeolite X, low silicon/aluminum ratio and hierarchical structure, could be a substantive advance, since it would lead to an active catalyst with an increased chemical processes rate as compared to the conventional zeolite-based catalysts. However, reaching the boundaries of the silicon/aluminium ratio in a LSX zeolite with hierarchical structure is a challenge that few researchers are currently undertaking. Parsapur and Selvam have prepared LTA-type zeolite using dimethyloctadecyl ammonium chloride (DOAC) as a structure-directing agent (SDA) [21]. Previously, we have shown that the use of sodium dodecylbenzene sulfonate (SDBS) as templating agent allows to introduce mesoporosity in FAU zeolites. However, the silicon/aluminum molar ratio had values around 1.5 [19]. For this reason, the aim of this work is focused on synthesizing a hierarchical structure that maintains the FAU framework but with a silicon/aluminum molar ratio close to 1.0. In other words, to synthesize mesoporous Low Silica X zeolite (MLSX).

2. Experimental

2.1. Materials

The materials used in this work were sodium hydroxide (NaOH, reagent grade, ≥98%), sodium dodecylbenzene sulfonate (SDBS, $C_{18}H_{29}NaO_3S$, technical grade) and oleic acid (technical grade 90%) supplied by Sigma Aldrich, sodium silicate (Na_2SiO_3, neutral solution technical grade) and potassium hydroxide (KOH, 85% for analysis) provided by Panreac, and sodium aluminate ($NaAlO_2$, RE- Pure) provided by Carlo Erba.

2.2. Synthesis

Low Silica X zeolite (LSX) was synthetized according to the hydrothermal method developed on previous studies [6]. The precursor gel was prepared with a sodium and potassium hydroxides dissolution on a batch reactor with Mili-Q water followed by the addition of sodium aluminate. Finally, the sodium silicate was slowly added to the solution. Aging and crystallization stages were carried out at the same temperature, 343 K. The solid product was filtered, washed with 0.01 M KOH aqueous solution to avoid protonation and dried at 373K overnight. MLSX zeolite, with mesoporosity, was synthesised by using the same method employing SDBS (molecular size: 2.26 × 0.52 × 0.80 nm [22]) as templating agent (Scheme 1).

SDBS was added to the synthesis gel after the solution of the sodium aluminate. The stirring mixture time (150 rpm), named as dissolution time of SDBS (t_{SDBS}), was 1 and 24 h for the M_1LSX_{SDBS} and $M_{24}LSX_{SDBS}$ zeolites, respectively.

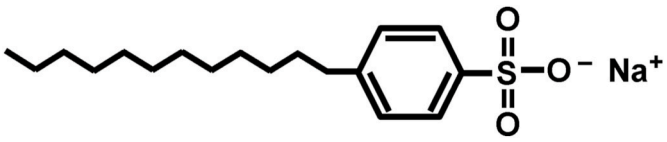

Scheme 1. Sodium dodecyl benzene sulphonate molecule.

The LSX synthesis gel composition was $1Al_2O_3$:$2.2SiO_2$:$5.5Na_2O$:$1.6K_2O$:$93.6H_2O$. This was obtained employing: 44.8 g of Na_2SiO_3, 14.9 g of $NaAlO_2$, 28.9 g of NaOH, 19.7 g of KOH and 161.6 g of H_2O. In the MLSX synthesis the surfactant concentration was 8 times its critical micelle concentration (CMC), which has a value of 2.73 mM at 298K [23]. The amount of SDBS was 1.5 g for a synthesis with 200 g of water.

Different calcinations conditions were employed to remove the surfactant from the material structure. These are shown in Table 1. Where T_0 is the initial temperature; t_1 is the time to reach the T_1 and t_2 is the isotherm time at T_1.

Depending on the calcination time and temperature conditions, these methods have been classified from harder to softer: C1>C2>C3>C4>C5.

At this point it is necessary to mention that the method C1 was discarded because it produced an appreciable destruction of the crystalline structure, so the results showed below only are referred to the other calcination methods.

2.3. Characterization

Different techniques for the characterization of zeolites were used to study the different properties of the synthetized materials. X-ray diffraction (XRD) patterns were recorded on a SIEMENS-D501 diffractometer with CuKα1 radiation for 2θ between 5° and 50° scanning range and a step size of 0.1. Chemical composition was determined using X-ray fluorescence (XRF) in an Aχios instrument. ^{27}Al and ^{29}Si MAS NMR spectra were obtained on a Bruker AV 400WB spectrometer with a 4 mm Bruker probe at spinning rates of 12 kHz with a recycle delay of 5 s, in both cases, with frequencies of 104.26 MHz and 79.49 MHz for ^{27}Al and ^{29}Si, respectively. Pulse width of 4.5μs and 4μs was used for ^{29}Si and ^{27}Al NMR analysis, respectively. Scanning and transmission electron micrographs (SEM and TEM) were recorded at the ICTS National Electronic Microscopy Centre from the Complutense University of Madrid with the JEOL JSM 7600F and the JEOL JEM 1400 microscopes, respectively. Adsorption-desorption isotherms of N_2 were obtained at 77 K using a MICROMERITICS ASAP 2020. Zeolites were degassed at 573 K for 3 h. Total specific surface area and volume of pores were determined using the Brunauer-Emmett-Teller (BET) equation and the single-point method ($p/p_0 = 0.99$), while the pore size distribution (PSD) curves were calculated from the desorption branch by the Barret-Joyner-Halends (BJH) method. Micropore volume were calculated using the *t*-plot method. The thermogravimetric (TG) and derivative thermogravimetric (DTG) measurements were conducted on a Setaram Labsys EVO apparatus from a temperature of 303–973 K under air flow with a heating rate of 10 K/min.

2.4. Catalytic activity

Oleic acid was used as probe molecule to examine the deoxygenation activity. Deoxygenation of oleic acid was carried out in a fixed bed at 698 K in continuous nitrogen flow (20 mL min^{-1}) at atmospheric pressure. Previously, the zeolite (2 g) was calcined *in situ* for 1 h at the reaction temperature, 698 K, in nitrogen stream. The reactants (oleic acid at 5 wt% in tetrahydrofuran) were continuously fed to the reactor at the

Table 1
SDBS removal conditions.

	T_0 (K)	t_1 (h)	T_1 (K)	t_2 (h)
C1	293	6.0	823	3.0
C2	293	1.0	773	3.0
C3	293	6.0	773	1.0
C4	293	1.0	773	0.75
C5	293	1.0	748	0.75

desired flow rate (0.1 ml/min) by a HPLC pump (Lab Alliance Serie III Digital). THF was used as solvent since it is able to dissolve both polar and non-polar products which appear in the wide products distribution.

Different samples were taken for monitoring the evolution of the reaction over time on stream (TOS) of: 30, 60, 90, 120, 150, 180, 210, 240 and 270 min. These samples were analysed by Gas Chromatography in a Varian CP-3800 equipped with a capillary column TRB-5 (60m × 0.25mm × 0.25 μm) and flame ionization detector (FID). The values of conversion of oleic acid and yield were obtained using the following equations:

$$X_{\text{oleic acid}} = \left(F^{0}_{\text{oleic acid}} \text{ e } F_{\text{oleic acid}}\right) / F^{0}_{\text{oleic acid}}\ 100 \quad (1)$$

$$Y_{\text{Product}} = F_{\text{Product}} / F^{0}_{\text{oleic acid}}\ 100 \quad (2)$$

$$Y_{\text{Product}} = \sum F_{\text{DOproducts}} / F^{0}_{\text{oleic acid}}\ 100 \quad (3)$$

where $F^{0}_{\text{oleic acid}}$ (mol·s^{-1}) is the molar flow rate of oleic acid at the inlet, $F_{\text{oleic acid}}$ (mol·s^{-1}) and F_{product} (mol·s^{-1}) are the molar flow rate of oleic acid and the molar flow rate of the different products at the outlet of the reactor, respectively. Finally, $\Sigma F_{\text{DOproducts}}$ (mol·min^{-1}) is the sum of the molar flow rate of deoxygenation products: saturated and unsaturated hydrocarbons.

3. Results and discussion

In previous works, we have used SDBS to introduce mesoporosity in the X zeolite but with a silicon/aluminum molar ratio of 1.2–1.5 [19]. The present work is a continuation of the previous one but obtaining a different zeolite, with the same FAU framework but a lower Si/Al ratio for which different synthesis conditions are required. The synthesis of LSX zeolite (Si/Al = 1.0) is more complex since it involves the presence of potassium, shorter time at lower temperature and a higher aluminum content in the synthesis media, all of which contribute to the thermal stability decrease. This zeolite is very interesting since the potential use of the zeolite is increased lowering the silicon/aluminum molar ratio, due to the higher amount of active sites. These are acid-base pairs where the cations are Lewis acids and the negative charge density on the framework oxygens are Lewis bases. In addition, the ionic exchange capacity is also increased. All together with the advantage of the hierarchical structure makes for a very interesting material. SDBS was used due to the previous good results, but a deeper study of the SDBS removal by calcination was carried out in this work and the resultant zeolites were analysed by different techniques as ^{27}Al and ^{29}Si MAS NMR or Scanning and Transmission Electronic Microscopy. The synthesis of mesoporous LSX zeolite supposed to increase 26% the active sites (as cationic positions) respect to the previous mesoporous zeolite. Here there are two alkaline cations (Na^+ and K^+) which can act as cationic bridge ($I^-X^+S^-$) between the anionic silicate and aluminate species (I^-) and the anionic surfactant molecules (S^-) but without affecting the zeolite crystallinity.

The removal of the SDBS after the synthesis was carried out by oxidant atmosphere calcination in air, extending the study of calcination conditions with respect to previous work. The decomposition temperature of the SBDS was around 750 K according to the TG analysis (Fig. 1). Therefore, this was the lowest temperature employed in the removal process (C5 conditions). The rest of the methods used higher temperatures.

3.1. X-ray diffraction (XRD) patterns/structure

Fig. 2 shows the X ray diffraction patterns of the synthesised zeolites and an amorphous sample before crystallization (dot line). The amorphous halo of this sample (a shoulder between 17.5° and 36°, centred at 28.5°) was taken as a reference of zeolite without crystallinity. In addition, the baseline in each diffractogram is represented by a straight

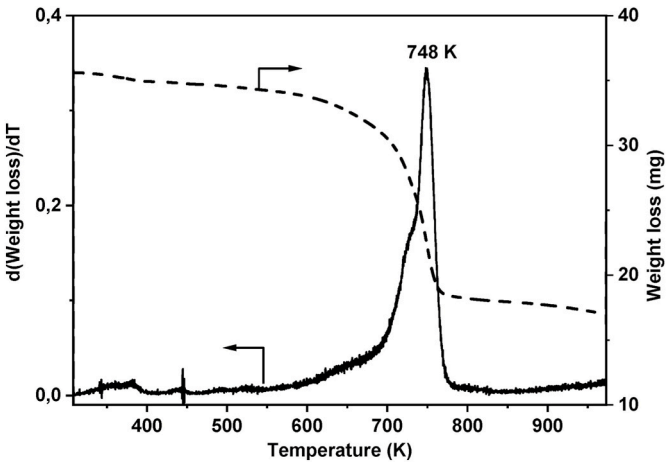

Fig. 1. TG/DTG plots of SDBS.

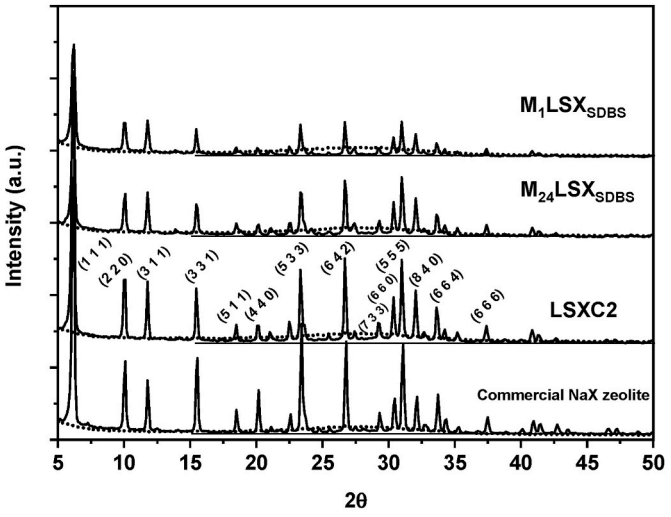

Fig. 2. X-Ray Diffraction of the as-synthesised zeolites (dot line displays the halo amorphous) with the *hkl* reflections.

line. LSXC2 zeolite (LSX zeolite calcined by the method C2) has been taken as a 100% crystallinity (peak area at 26.6 2θ) reference to see more clearly the effect of the surfactant on the synthesized materials.

All the zeolites XRD profiles showed the characteristic peaks of the FAU framework which are, as expected, coincident with the ones obtained for the commercial NaX zeolite supplied by Sigma-Aldrich. However, the intensity of the reflections was lower than the corresponding to the commercial NaX zeolite which could result in lower crystallinity. It is important to note that in order to compare the intensity of the peaks between two zeolites, it is necessary that both have the same composition. Zeolites were synthesised with potassium in the media, which, when incorporated into the structure, can attenuate the intensity of XRD profiles due to its larger size as compared to sodium, without affecting crystallinity. In addition, the presence of SDBS in the zeolites could contribute to reduce the peak intensity of mesoporous samples. The absence of halo amorphous confirmed that the as-synthesised zeolites were crystalline. Therefore, the use of SDBS in the synthesis media did not affect the zeolite framework. On the other hand, considering the area under the peak at 26.6° as reference to calculate the crystallinity, the $M_{24}LSX_{SDBS}$ zeolite (peak area 800, crystallinity 74%) showed higher crystallinity than M_1LSX_{SDBS} zeolite (peak area 440, crystallinity 40%). Therefore, it can be inferred that a longer t_{SDBS} improved the crystallinity of the zeolite, as micelles formation is favored.

As mentioned above, different temperatures were used during the

calcination step (Table 1) to remove the surfactant after the synthesis. Fig. 3 shows the XRD patterns of the $M_{24}LSX_{SDBS}$ zeolites after calcination treatment. All the zeolites presented the characteristic peaks of the FAU zeolites but with different intensities. However, the amorphous halo of the zeolites was higher for calcined sample at 773K for 3 h ($M_{24}LSX_{SDBS}C2$, crystallinity 56%) as compared with the samples calcined with softer methods (0.75 h at 773K, crystallinity above 80%), $M_{24}LSX_{SDBS}C4$ and $M_{24}LSX_{SDBS}C5$ indicating lower crystallinity. In general, the peak intensity was lower for the calcined zeolites as compared with non-calcined samples, indicating the presence of smaller crystalline domains after the thermal treatment. In no case does the crystalline structure of the zeolite completely collapse after the surfactant removal.

3.2. Composition

Tables 2 and 3 show the results of the XRF analysis and textural properties of the as-synthesised and calcined zeolites.

As it can be seen in Tables 2 and 3 the silicon/aluminum molar ratio was similar in all the zeolites (1.1–1.2), before and after the surfactant removal independently of the calcination method. XRF analysis gives information about the bulk composition of the samples regardless silicon-aluminum bond type. However, the silicon/aluminum molar ratio corresponding to the zeolitic structure can be determined by MAS NMR analysis. The structure of Si atoms nearby Al atoms was identified by the ^{29}Si MAS NMR technique. In zeolites, with a 3D structure, the predominant species are Q4 (Si(–O–)$_4$). Moreover, the ^{29}Si MAS NMR is also sensitive to atoms in the second coordination sphere providing information about the zeolite framework order, indicating the number of aluminium atoms to which oxygen atom is bonded, four (Q^4(4Al)), three (Q^4(3Al)) … until none (Q^4(0Al)). Therefore, the zeolite framework silicon/aluminum molar ratio can be calculated according to equation (4) [24].

$$Si/Al = \sum A_{m,n} / \sum (m/n) A_{m,n} \quad (4)$$

$A_{m,n}$ is the area of peak corresponding to Si(nAl) unit. Fig. 4 shows the ^{29}Si MAS NMR spectra. The analysis of ^{29}Si MAS NMR showed a single ^{29}Si resonance peak at 85–86 ppm (Si(4Al)) with a little shoulder around 90 ppm (Si(3Al)) which was more significant in the calcined zeolites. The silicon/aluminum molar ratio calculated from equation (4) was 1.02 for the zeolites LSXC2 and $M_{24}LSX_{SDBS}$. For the $M_{24}LSX_{SDBS}C3$ zeolite the ratio was slightly higher, reaching a value of 1.08 whereas for the $M_{24}LSX_{SDBS}C2$ the ratio increased to 1.18. Therefore, the main conclusion is that structural silicon/aluminum molar ratio was very close to the limit value established by Lowenstein's rule. The difference with the values calculated by XRF could be due to the characteristic of each analysis and/or to the presence of a negligible amorphous phase not detected by XRD analysis.

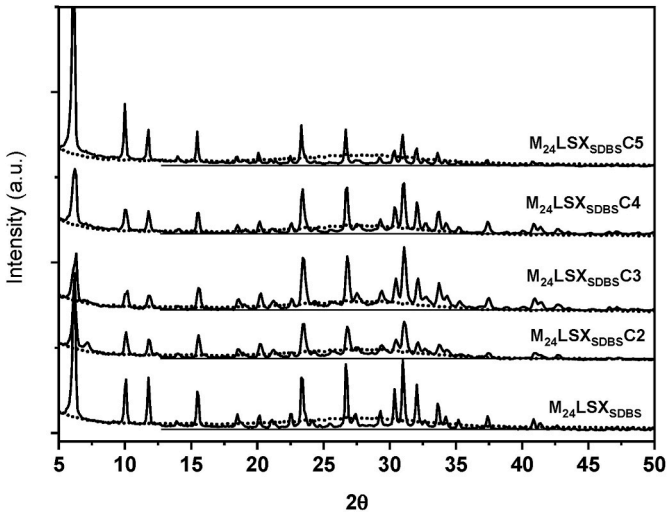

Fig. 3. X-Ray Diffraction patterns of the calcined zeolites.

On the other hand, the ^{27}Al MAS NMR provides information about the different framework and extra-framework aluminum species in the zeolite. Fig. 5 displays the ^{27}Al MAS NMR spectra of the LSXC2, $M_{24}LSX_{SDBS}$, $M_{24}LSX_{SDBS}C2$ and $M_{24}LSX_{SDBS}C3$ zeolites. These spectra showed only a single Al signal at 61 ppm which is typical of tetra-coordinated zeolitic Al. Therefore, the presence of extra-framework aluminum, at 0 ppm, was not observed. However, the calcined zeolites showed a shoulder at δ_{iso} = 55 ppm which might be separated by deconvolution as Fig. 5 displays This signal may be related with different Al^{IV} environments such as distorted Al species [25] connected with the amorphous phase generated during the calcination [26]. Similar behaviour was observed by Van Aelst et al. [27] in USY zeolites desilicated using NH_4OH. In the $M_{24}LSX_{SDBS}C2$ zeolite, the broadening of this peak was more significant due to the higher crystallinity loss. However, in $M24LSX_{SDBS}C3$ (crystallinity 72%) the loss of crystallinity is not so evident. This signal at 55 ppm can also be assigned to partially coordinated Al framework (denoted as Al(IV)-2) [28]. Therefore, the removal of SDBS resulted in an increase of the Al(IV)-2 framework species due to the increase of tetrahedral aluminum on the surface. These tetrahedral aluminum are completed with –OH groups, increasing the presence of distorted AlI(IV) species, without a clear loss of crystallinity when the calcination conditions were milder.

3.3. Mesoporosity

Table 2 shows the textural properties of the zeolites. Specific surface area of the as-synthesised zeolites (with the remaining SDBS) was lower than the calcined LSX zeolites due to the presence of surfactant in the pores. The decrease in the M_1LSX_{SDBS} reached 13% whereas for $M_{24}LSX_{SDBS}$ was only 5%. The same trend was observed in the micropore volume with a reduction of 15% and 7% for M_1LSX_{SDBS} and $M_{24}LSX_{SDBS}$, respectively. This behaviour is linked to the crystallinity, higher when the t_{SDBS} was longer. In the synthesis with SDBS, the total volume of pore was increased in the range 8–11%, despite the decrease in micropore volume. Especially important was the mesopores volume increase, which was doubled in both zeolites as compared to LSX, indicating that some of the surfactant was removed during the washing stage or even during degassing at 573K prior to nitrogen adsorption/desorption at 77K.

Fig. 6 A and B displays the N_2 adsorption-desorption isotherms at 77K and the pore size distribution, respectively. Pore size distribution is shown from size starting at 50 Å because of the forced closure of the isotherm desorption branch owing to a sudden drop of adsorbed volume in the p/p_0 range 0.41–0.48. This effect is referred to as tensile strength effect and it is typical of zeolites [29]. This can lead to misinterpretation of the pore size distribution concluding that zeolites have a narrow pore size distribution centred on 40 Å (d_{TSE} = 38 Å, according to the BJH model).

According to the IUPAC classification [30], the shape of the N_2 adsorption-desorption isotherm for the LSX zeolite belongs to the type I with H4 hysteresis loop, typical of microporous materials. However, the LSX zeolites synthesised with SDBS showed an isotherm belonging to type I + II, with an H3 hysteresis loop, related to mesoporous materials. As it can be seen in Fig. 6 B, these zeolites presented a wider pore size distribution in the mesopores range, due to the presence of the SDBS during the synthesis. Part of the surfactant was removed during the washing step leading to a wide pore size distribution, with a maximum around 200 Å for the M_1LSX_{SDBS} zeolite and around 280 Å for the $M_{24}LSX_{SDBS}$ zeolite. Therefore, the pore size distribution was narrower for longer t_{SDBS} ($M_{24}LSX_{SDBS}$). Zeolite LSX showed a small shoulder at high pore diameter values associated with intraparticle cavities.

SDBS removal by calcination also produced a reduction of the

Table 2
Textural properties of the as-synthesised zeolites.

	LSX	LSXC2	$M_{24}LSX_{SDBS}$	M_1LSX_{SDBS}
Si/Al molar ratio	1.15	1.14	1.15	1.12
Unit cell[a]	$Na_{64}K_{31}$ $(SiO_2)_{103}(AlO_2)_{89}$	$Na_{63}K_{30}$ $(SiO_2)_{102}(AlO_2)_{89}$	$Na_{69}K_{32}$ $(SiO_2)_{103}(AlO_2)_{89}$	$Na_{71}K_{33}$ $(SiO_2)_{102}(AlO_2)_{90}$
S_{BET} (m^2/g)	715	640	680	625
$V_{micropore}$ (cm^3/g)	0.253	0.229	0.236	0.216
$V_{mesopore}$[b] (cm^3/g)	0.049	0.037	0.100	0.11
V_{total} (cm^3/g)	0.302	0.266	0.336	0.326
$V_{mesopore}/V_{total}$ (%)	16	14	30	34

[a] Unit cell of faujasite: Si + Al = 192 atoms.
[b] $V_{mesopore} = V_{total} - V_{micropore}$.

Table 3
Textural properties of the calcined zeolites.

	$M_{24}LSX_{SDBS}C2$	$M_{24}LSX_{SDBS}C3$	$M_{24}LSX_{SDBS}C4$	$M_{24}LSX_{SDBS}C5$
Si/Al molar ratio	1.15	1.14	1.16	1.12
Unit cell[a]	$Na_{67}K_{32}$ $(SiO_2)_{103}(AlO_2)_{89}$	$Na_{66}K_{32}$ $(SiO_2)_{102}(AlO_2)_{90}$	$Na_{71}K_{32}$ $(SiO_2)_{103}(AlO_2)_{89}$	$Na_{80}K_{38}$ $(SiO_2)_{101}(AlO_2)_{91}$
S_{BET} (m^2/g)	170	325	505	570
$V_{micropore}$ (cm^3/g)	0.05	0.106	0.172	0.194
$V_{mesopore}$[b] (cm^3/g)	0.165	0.14	0.125	0.119
V_{total} (cm^3/g)	0.215	0.246	0.297	0.313
$V_{mesopore}/V_{total}$ (%)	77	57	42	38

[a] Unit cell of faujasite: Si + Al = 192 atoms.
[b] $V_{mesopore} = V_{total} - V_{micropore}$.

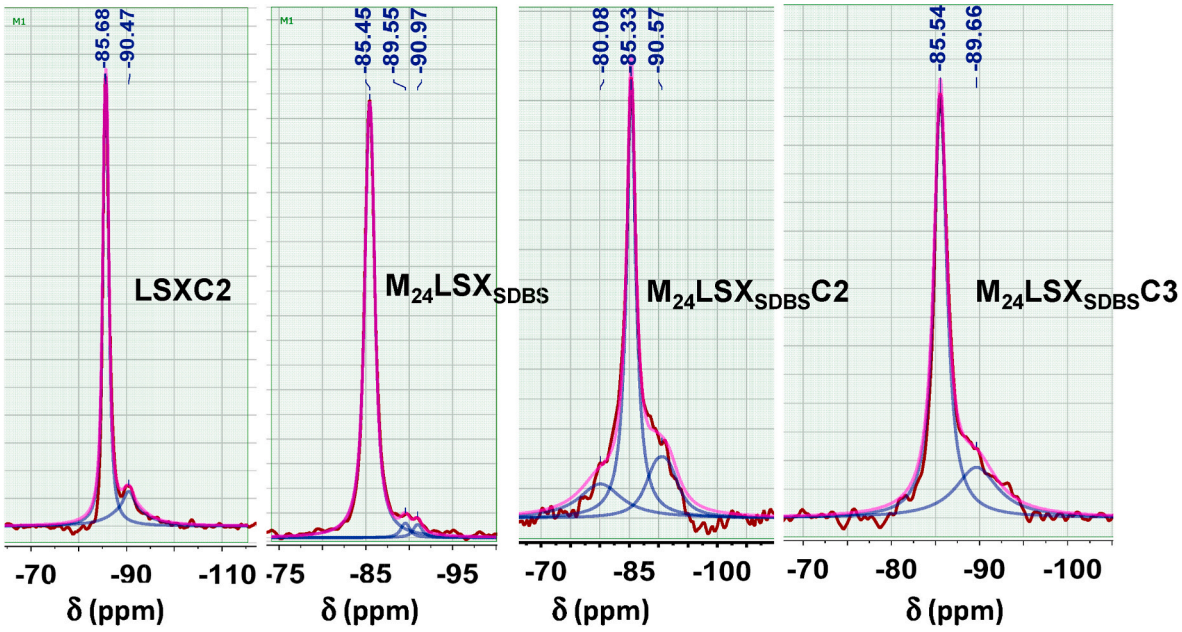

Fig. 4. ^{29}Si MAS NMR spectra and deconvolution curves of the zeolites: LSXC2, $M_{24}LSX_{SDBS}$, $M_{24}LSX_{SDBS}C2$ and $M24LSX_{SDBS}C3$.

specific surface area and micropore volume. This decrease was related to the loss of crystallinity as it was seen in the XRD analysis. The decrease depended on the conditions used in the removal of the surfactant. Harder conditions led to greater reduction, specific surface area reduction was 75% for the C2 method, 52% for the C3 method, 26% for the C4 method and 16% for the C5 method. Similar behaviur was observed in the micropore volume variation. Again, the reduction in surface area was linked to a mesopore volume increase with a $V_{mesopores\ calcined}/V_{mesoporoes\ as\text{-}synthesised}$ of 1.7, 1.4, 1.3 and 1.2 times for the C2, C3, C4 and C5 methods respectively. The initial textural properties were almost recovered when the softer C5 method was employed. Fig. 7 A and B shows the N_2 adsorption-desorption isotherms at 77K and pore size distribution of the calcined zeolites, respectively. This zeolite exhibited a type I isotherm, typical of microporous materials, characterized by a rapid rise of the adsorbed nitrogen at low relative pressures ($p/p_0 < 0.2$) followed by a plateau up to relative pressures of 0.8–0.9 with a final rise due to the interparticle voids filling. On the other hand, the isotherms of the calcined zeolites belong to type I + II, but the contribution of each type changed depending on the calcination method. These isotherms presented a first part similar to type I, with the filling of the micropores at low relative pressures ($p/p_0 < 0.2$), followed by a continuous rise (type II), more or less pronounced depending on the calcination method, which corresponds to the filling of the mesopores. In the final part, they showed the typical rise due to intraparticle porosity, which was more pronounced in the zeolite $M_{24}LSX_{SDBS}C2$. The contribution of each type to the overall isotherm changed according to the method employed for

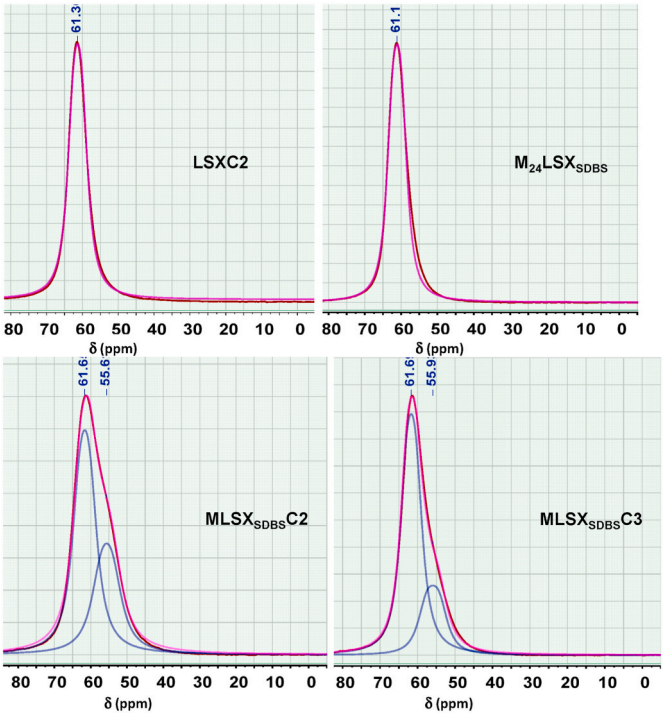

Fig. 5. ^{27}Al MAS NMR spectra and deconvolution curves of the zeolites: LSXC2, $M_{24}LSX_{SDBS}$, $M_{24}LSX_{SDBS}C2$ and $M24LSX_{SDBS}C3$.

the removal of SDBS, being the contribution of type I higher in the $M_{24}LSX_{SDBS}C5$ zeolite (soft calcination). Pore size distributions and their corresponding peak deconvolution are showed in Fig. 8. The pore size distribution shows the development of mesoporosity due to the removal of SDBS. $M_{24}LSX_{SDBS}C5$ zeolite showed almost the same pore size distribution than the $M_{24}LSX_{SDBS}$ zeolite, since the C5 calcination (up to 748K) method was not enough to completely remove the SDBS. However, the $M_{24}LSX_{SDBS}C4$ zeolite calcined at 773K showed a wider pore size distribution centred at 230 Å due to the total removal of the SDBS. On the other hand, the zeolite $M_{24}LSX_{SDBS}C3$, with a low heating rate during the calcination, showed a bimodal distribution with the maximum around 290 Å, like the zeolite before calcination, and a new peak centred at 80 Å due to surfactant removal. Nevertheless, zeolite $M_{24}LSX_{SDBS}C2$ did not show this clear bimodal distribution due to the collapse of the pores for the longer calcination time at 773 K (3 h), giving a distribution with a maximum centred over 160 Å. This distribution was fitted by deconvolution to the sum of the peaks corresponding to the pores already present in the as-synthesised zeolite (>200 Å) and those that would come from the collapse of smaller pores (<100 Å), which are centred over 140 Å.

The development of mesoporosity dependent on the calcination method used to remove the SDBS, being necessary, at least, a temperature of 773K and short time at this temperature. These are the conditions of the C3 and C4 methods, which allow obtaining a zeolite with mesoporosity and without appreciable loss of crystalline structure. The effect of the calcination on the MLSX porous structure was difficult to finely control, leading to a multimodal pore size distribution or a wider pore size distribution. However, this mesoporosity was not related to an ordered structure, as in MCM41 or SBA-15, since the low-angle XRD pattern (not shown) did not exhibit any shoulder. Therefore, the structure would be more similar to that of disordered mesoporous carbons.

The shape of the SDBS micelles above 5 CMC would be, according to the literature, prolate ellipsoid [31] or hollow sphere [32]. Therefore, a disordered mesoporous structure is formed, as no rod-like micelles develop that could lead to a structure similar to that of MCM41 or SBA15. Scheme 2 represents how the surfactant is introduced into the zeolite during the crystallization and the mesoporous are produced during the calcination.

3.4. Scanning Electronic Microscopy analysis

Fig. 9 displays Scanning Electronic Microscopy (SEM) images for the LSX, $M_{24}LSX_{SDBS}$ and $M_{24}LSX_{SDBS}C3$ zeolites. All zeolites presented spherical shaped particles formed by crystalline aggregates with smooth faces. Amorphous material was hardly noticeable indicating the high crystallinity of the zeolites.

Fig. 10 shows SEM images obtained for an accelerating voltage of 1 kV with a magnification 100000X, which makes it possible to observe the surface of the zeolite particles. SEM micrographs of zeolites showed sharp and clear edge of the zeolite crystalline grains. Again, the LSXC2 zeolite was taken as reference, showing a smooth surface whereas the $M_{24}LSX_{SDBS}C3$ zeolite presented a rougher surface. In this zeolite, a series of heterogeneously distributed black spots can be clearly distinguished on the surface, which were associated with the entry cavities of the mesopores produced during surfactant removal. The distribution of these cavities was irregular, indicating a disordered mesoporous structure. The SEM images were similar to the corresponding to USY zeolite

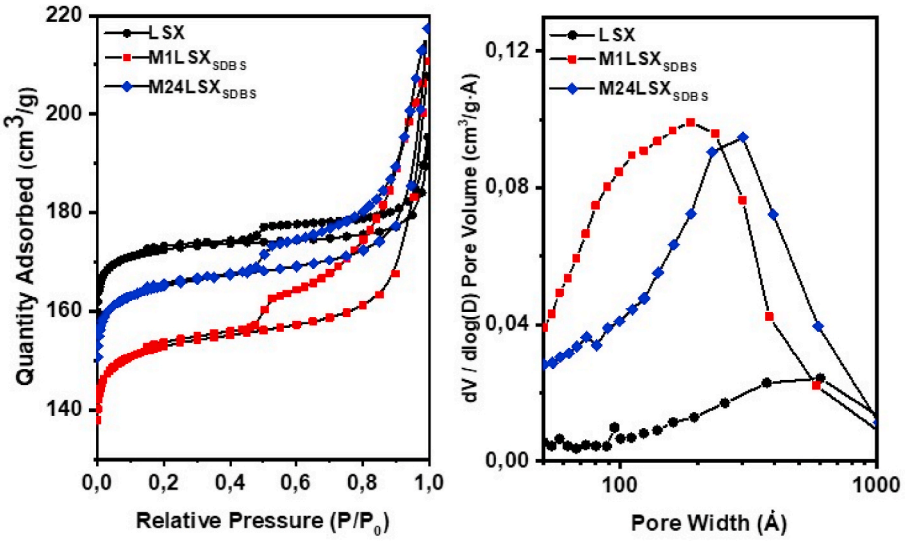

Fig. 6. N_2 adsorption-desorption at 77 K (A) and pore size distribution (B) of LSX, $M1LSX_{SDBS}$ and M24 LSX_{SDBS} zeolites.

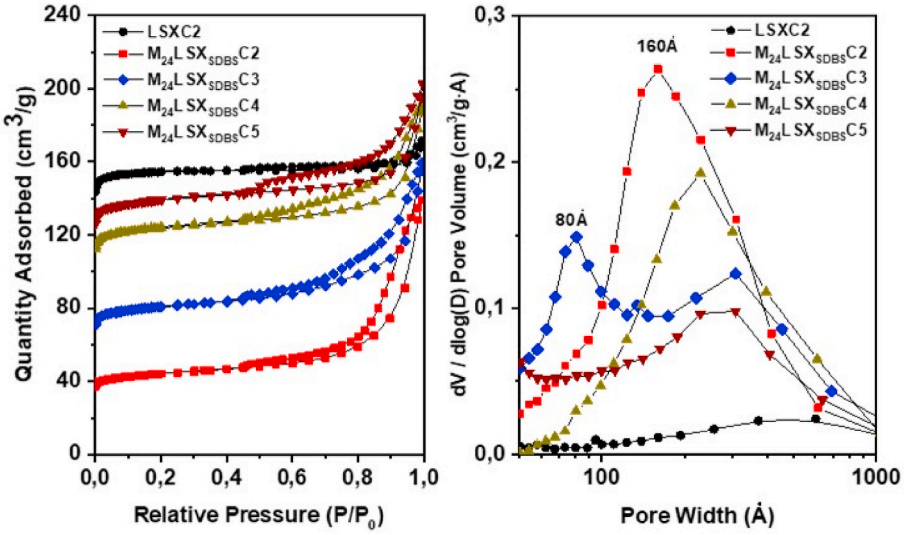

Fig. 7. N_2 adsorption-desorption at 77 K (A) and pore size distribution (B) of LSXC2, $M_{24}LSX_{SDBS}C2$, $M_{24}LSX_{SDBS}C3$, $M_{24}LSX_{SDBS}C4$and $M_{24}LSX_{SDBS}C5$.

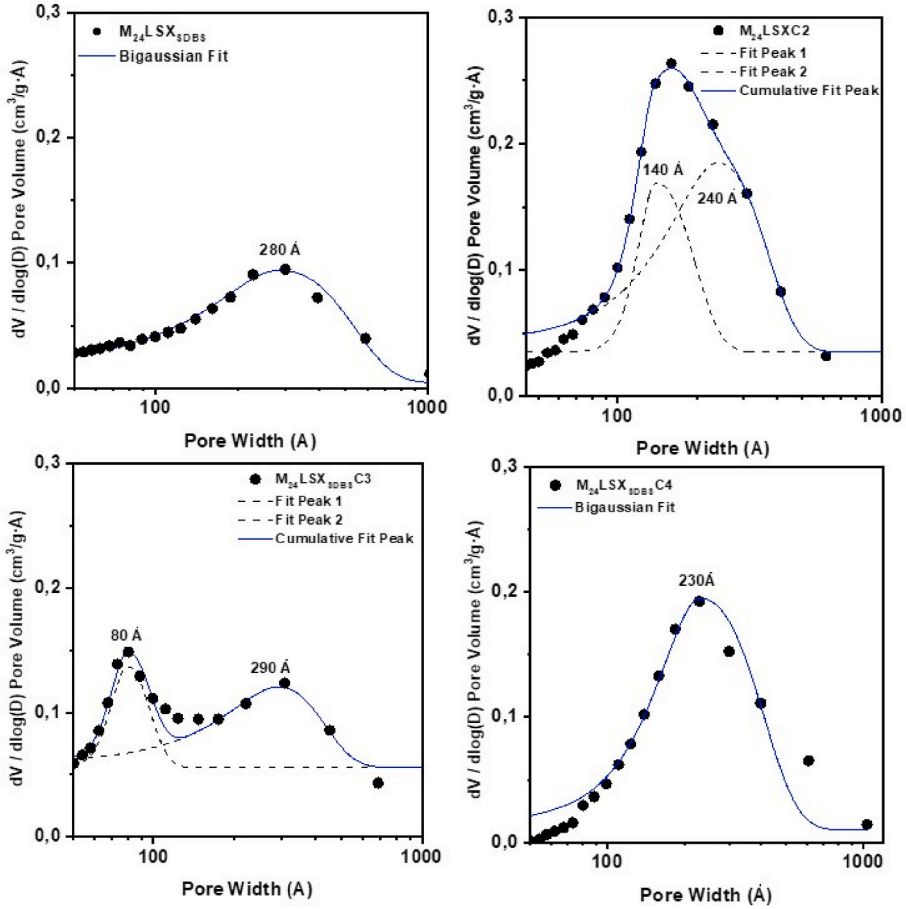

Fig. 8. Deconvolution results of the pore size distributions of the zeolites: $M_{24}LSX_{SDBS}$, $M_{24}LSX_{SDBS}C2$, $M_{24}LSX_{SDBS}C3$ and $M_{24}LSX_{SDBS}C4$.

where some mesoporosity is formed during the dealumination process [33]. However, dealumination was not produced during the removal of the SDBS in the zeolites studied in this work since the silicon/aluminum molar ratio did not change.

Although the XRD analysis showed a high crystallinity, with no remarkable impurities of other phases, some curious images were obtained in the SEM analysis, where several morphologies could be observed. As an example, Fig. 11 shows different crystallites morphologies, the octahedral typical of LSX zeolite along with cubic crystals, characteristic of A zeolite, upper part, and pellets morphology of hydroxysodalite crystals, lower part [34]. These usually appear in the FAU zeolite synthesis.

Fig. 12 shows TEM images obtained with a tungsten filament operating at 120 kV. The TEM images of the $M_{24}LSX_{SDBS}C3$ zeolite (center

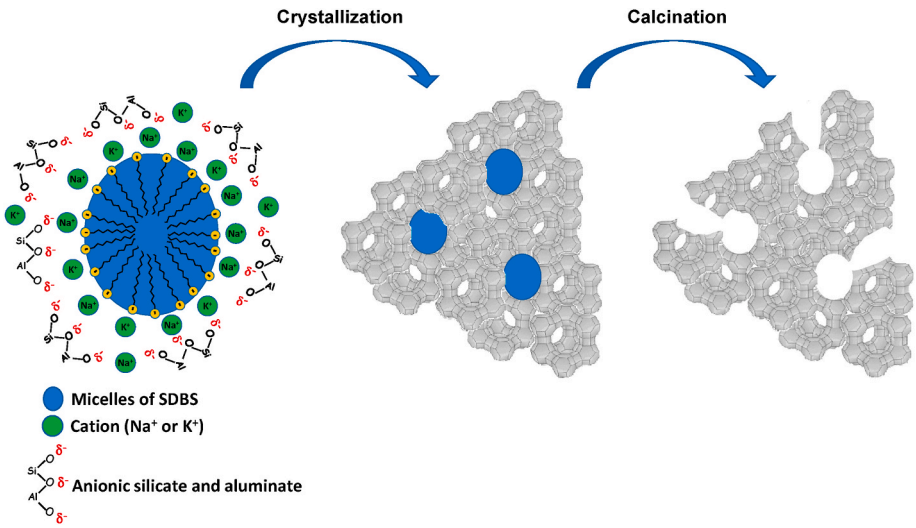

Scheme 2. Qualitative representation of the MLSX synthesis.

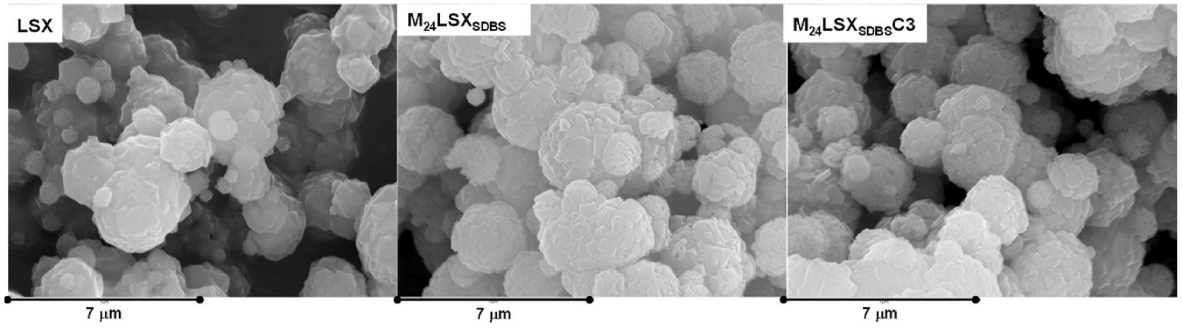

Fig. 9. SEM images of zeolites LSX, $M_{24}LSX_{SDBS}$ and $M_{24}LSX_{SDBS}C3$ with magnification 8000X.

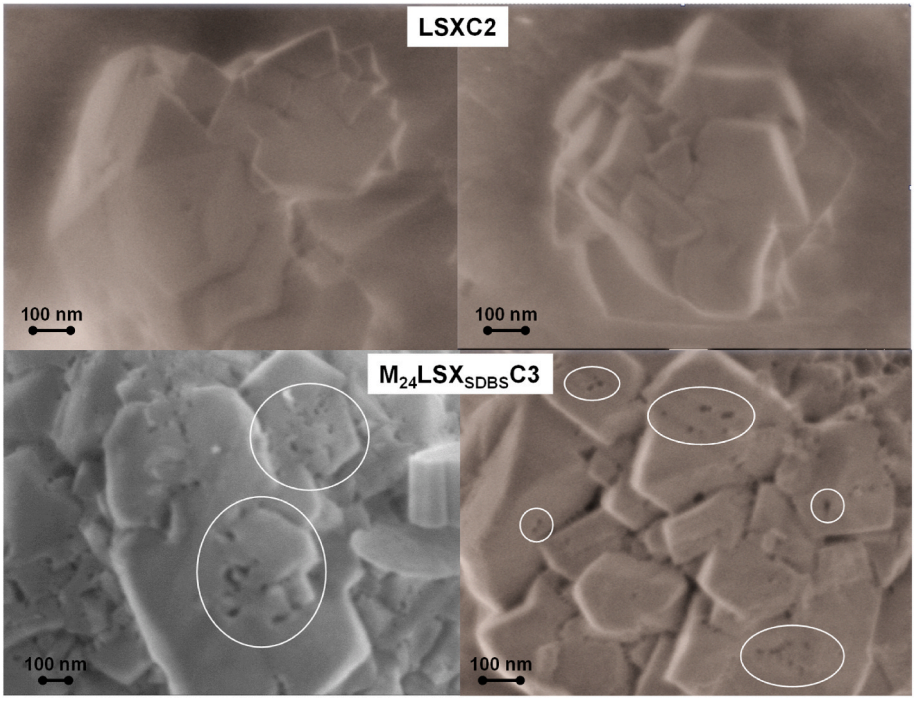

Fig. 10. SEM images of zeolites LSXC2 and $M_{24}LSX_{SDBS}C3$ with magnification 100000X.

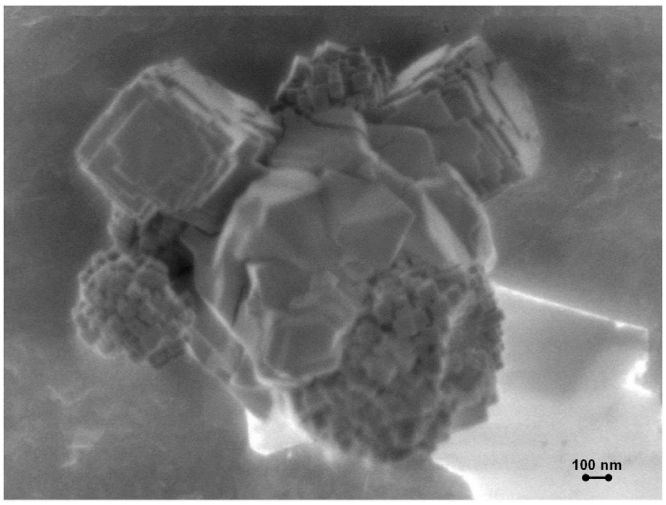

Fig. 11. SEM image of zeolites LSXC2 with magnification 40000X.

and right) showed clearly, more or less spherical voids in the nanoparticles. These areas presented different brightness indicating the presence of cavities and a disordered mesoporous. The presence of these cavities coincides with the shape of the SDBS micelles (Scheme 2). However, zeolite LSXC2 (left) did not show such areas. Therefore, these results support the successful generation of mesoporosity in the LSX zeolite.

3.5. Deoxygenation of oleic acid

Deoxygenation of oleic acid to produce sustainable aviation fuel (SAF) was used as a probe reaction to study the catalytic activity of LSX zeolite with and without mesoporosity. Products distribution was very wider including light and heavy biohydrocarbons, saturated and unsaturated, aromatic compounds, CO, CO_2, etc. The fraction from C_9 to C_{17} including paraffins (heptadecane, hexadecane, pentadecane, tetradecane … until nonane) and oleffins (heptadecenes, hexadecenes, pentadecens … until nonenes) was considered as representative of biojet fuel Fig. 13 shows the variation of conversion with the time on stream (TOS) for LSXC2 and $M_{24}LSX_{SDBS}C4$ zeolites. Although the conversion was maintained above 90% with both zeolites, the LSXC2 zeolite showed higher deactivation with a continuous decrease till 90%, whereas the mesoporous LSX zeolite presented a steady conversion of 100%. The hierarchical structure avoided the blockage of the pores allowing the access to active site, decreasing zeolite deactivation. This high resistance to deactivation is characteristic of the hierarchical porous zeolites.

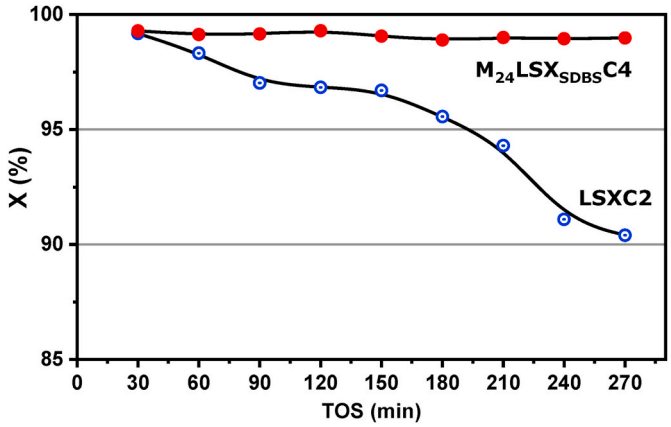

Fig. 13. Variation of the conversion of oleic acid with the time on stream (TOS). Reaction conditions: Temperature: 698 K, N_2 flow: 20mLmin^{-1}, solvent: THF and [Oleic acid]: 5 wt%.

Therefore, the MLSX zeolite was able to work longer time on stream maintaining the activity catalytic level.

Figs. 14 and 15 show the variation of the yield with the time on stream (TOS) for the LSXC2 and $M_{24}LSX_{SDBS}C4$ zeolite, respectively. The product distribution was grouped as C_9–C_{18} as representatives of bio jet fuel and C_6–C_8 as other biohydrocarbons. The yield of C_6–C_8 biohydrocarbons was very similar in both zeolites decreasing slightly with the TOS, reaching an average yield of 19%. However, the yield of C_9–C_{18} biohydrocarbons was clearly different. LSXC2 zeolite (Fig. 13) showed a similar behaviour to the yield of C_6–C_8 biohydrocarbons decreasing with the TOS due to the deactivation of the zeolite. The average yield of C_9–C_{18} for the 4.5 h of TOS was over 20%. However, the yield of bio jet fuel (C_9–C_{18}) was maintaining with the TOS reaching an average yield around 30% with the mesoporous zeolite (Fig. 14).Hierarchical structure allowed to produce larger biohydrocarbons chain due to the presence of mesoporous in the zeolite. Therefore, the $M_{24}LSX_{SDBS}C4$ zeolite was able to increase the production of bulky molecules. The main product among the biojet fuel fraction was C_{17} hydrocarbons (above 30%) indicating that the reaction mechanism involved deoxygenation reactions, as decarboxylation and decarbonylation. In addition smaller biohydrocarbons were also produced by catalytic cracking through zeolite Lewis acid and basic sites.

4. Conclusions

Mesoporous LSX zeolite (MLSX) synthesis was achieved using sodium dodecylbenzene sulfonate (SDBS), an anionic surfactant, as

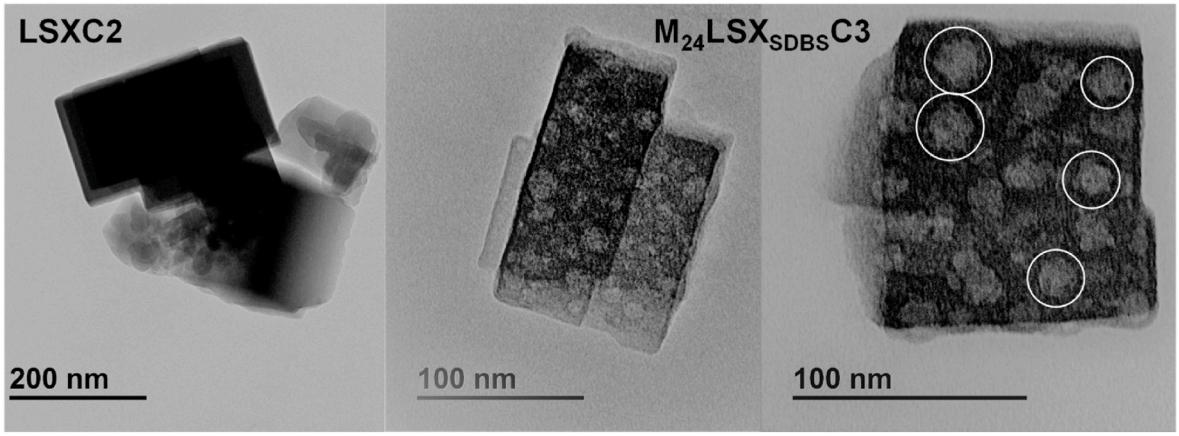

Fig. 12. TEM images of zeolites LSXC2 (left: x15000) and $M_{24}LSX_{SDBS}C3$ (centre: x40000 and right: x60000).

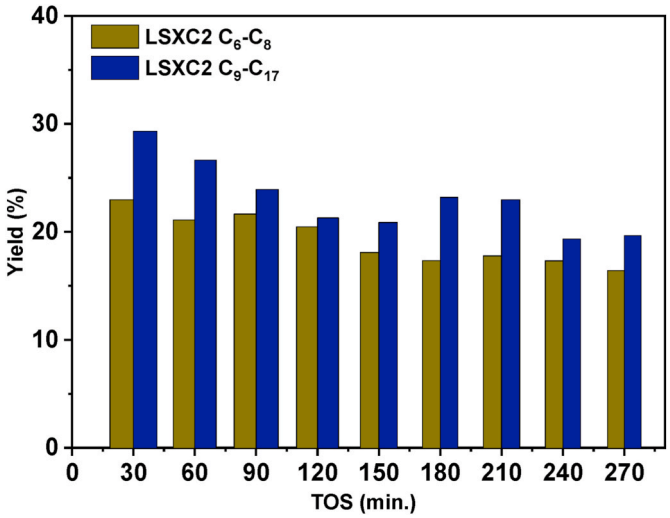

Fig. 14. Variation of the yield with the time on stream for the LSXC2 zeolite. Reaction conditions: Temperature: 698 K, N_2 flow: 20mLmin^{-1}, solvent: THF and [oleic acid]: 5 wt %.

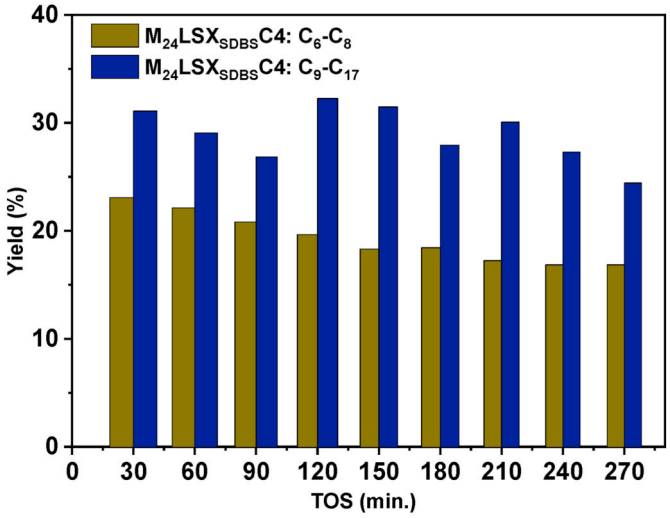

Fig. 15. Variation of the yield with the time on stream for the $M_{24}LSX_{SDBS}C4$ zeolite. Reaction conditions: Temperature: 698 K, N_2 flow: 20mLmin^{-1}, solvent: THF and [oleic acid]: 5 wt %.

template. A dissolution time of SDBS (t_{SDBS}) of 24 h was necessary to obtain LSX zeolite with high crystallinity. The presence of SDBS in the synthesis medium did not affect neither the FAU structure of the zeolite, obtaining high crystallinity, nor the silicon/aluminum molar ratio, maintaining a value near to the unity (<1.1), the limit of the Lowenstein's rule. The removal of the surfactant by calcination, reaching at least 723K with a short time at this temperature, was necessary for the mesoporosity development in the LSX zeolite. The heating rate determined the pore size distribution, resulting in a bimodal distribution (maxima at 80 Å and 290 Å) at low heating rate (1.3 K/min) and a unimodal distribution, with a maximum at 230A, at higher heating rate (8 K/min). The effect of the calcination in the porous structure was difficult to control leading to a wider pore size distribution. The removal of SDBS resulted in an increase of Al(IV)-2 species in the framework due to the increase of tetrahedral aluminium on the surface, as compared to the zeolite synthesised without SDBS (LSX zeolite).The optimum calcination method was the C4 resulting in a MLSX zeolite with a good balance between crystallinity and mesoporosity. The MLSX zeolite exhibited a disordered mesoporous structure with cavities formed by the removal of the spherical SDBS micelles. This MLSX zeolite showed higher catalytic activity, without deactivation, than the LSX zeolite, allowing to maintain the conversion close to 100% and increasing the production of C_9–C_{18} biohydrocarbons, representative compounds of sustainable aviation fuel (SAF). Therefore, the MLSX zeolite could be employed as a new catalyst for processing bulk molecules.

Declaration of competing interest

The authors declare that they have no known competing financial interests or personal relationships that could have appeared to influence the work reported in this paper.

Acknowledgements

This work was supported by the financial support of the Santander-UCM 2018 project (PR75/18). The authors want to acknowledge the assistance of the Luis Bru Electron Microscopy Centre and the research support centers (CAIs) in the Faculty of Chemistry of the Complutense University of Madrid for the XRD, XRF and NMR MAS analyses.

References

[1] Y. Li, L. Li, J. Yu, Inside Chem. 3 (2017) 928–949, https://doi.org/10.1016/j.chempr.2017.10.009.
[2] L. Bacakova, M. Vandrovcova, I. Kopova, I. Jirka, Biomater. Sci. 6 (2018) 974–989, https://doi.org/10.1039/c8bm00028j.
[3] D.W. Breck, Zeolite Molecular Sieves: Structure, Chemistry, and Use, John Wiley & Sons, Inc., New York, 1974.
[4] W. Löewenstein, Am Mineral 39 92 (1–2) (1954) 96.
[5] G.H. Kühl, Zeolites 7 (1987) 451–457, https://doi.org/10.1016/0144-2449(87)90014-5.
[6] M.D. Romero, J.M. Gómez, G. Ovejero, A. Rodríguez, Mater. Res. Bull. 39 (3) (2004) 389–400, https://doi.org/10.1016/j.materresbull.2003.10.018.
[7] S. Tontisirin, J. Porous Mater. 22 (2) (2015) 437–445, https://doi.org/10.1007/s10934-015-9912-1.
[8] C. Xue, X. Wei, Z. Zhang, Y. Bai, M. Li, Y. Chen, Materials 13 (2020) 3469. https://doi:10.3390/ma13163469.
[9] S. Tontisirin, Microporous Mesoporous Mater. 239 (2017) 123–129, https://doi.org/10.1016/j.micromeso.2016.09.051.
[10] R. Bai, Y. Song, Y. Li, J. Yu, Trends Chem. 1 (6) (2019) 601–611, https://doi.org/10.1016/j.trechm.2019.05.010.
[11] S. Mitchell, A.B. Pinar, J. Kenvin, P. Crivelli, J. Kärger, J. Pérez-Pariente, Nat. Commun. 6 (2015) 8633, https://doi.org/10.1038/ncomms9633.
[12] B. Wang, P.K. Dutta, Microporous Mesoporous Mater. 239 (2017) 195–208, https://doi.org/10.1016/j.micromeso.2016.10.008.
[13] W.W. Schwieger, A.G. Machoke, T. Weissenberger, A. Inayat, T. Selvam, M. Klumppa, A. Inaya, Chem. Soc. Rev. 45 (12) (2016) 3353–3376, https://doi.org/10.1039/C5CS00599J.
[14] J. Song, L. Ren, C. Yin, Y. Ji, Z. Wu, J. Li, F. Xiao, J. Phys. Chem. C 112 (23) (2008) 8609–8613, https://doi.org/10.1021/jp800598p.
[15] Y. Zhang, X. Han, S. Che, Chem. Commun. 55 (2019) 810–813, https://doi.org/10.1039/c8cc08281b.
[16] N. Suárez, J. Pérez-Pariente, F. Mondragón, A. Moreno, Microporous Mesoporous Mater. 280 (2019) 144–150, https://doi.org/10.1016/j.micromeso.2019.02.001.
[17] D. Verboekend, N. Nuttens, R. Locus, J. Van Aelst, P. Verolme, J.C. Groen, J. Pérez-Ramírez, B.F. Selsa, Chem. Soc. Rev. 45 (12) (2016) 3331–3352, https://doi.org/10.1039/C5CS00520E.
[18] T. Yutthalekh, C. Wattanakit, C. Warakulwit, W. Wannapakdee, K. Rodponthukwaji, T. Witoon, J. Limtrakul, J. Clean. Prod. 142 (2017) 1244–1251, https://doi.org/10.1016/j.jclepro.2016.08.001.
[19] J.M. Gómez, E. Díez, A. Rodríguez, M. Calvo, Microporous Mesoporous Mater. 270 (2018) 220–226, https://doi.org/10.1016/j.micromeso.2018.05.029.
[20] B. Reiprich, T. Weissenberger, W. Schwieger, A. Inayat, Front. Chem. Sci. Eng. 14 (2) (2020) 127–142, https://doi.org/10.1007/s11705-019-1883-3.
[21] R.K. Parsapur, P. Selvam, Sci. Rep. 8 (1) (2018) 1–13, https://doi.org/10.1038/s41598-018-34479-4.
[22] K. Yang, L. Zhua, B. Xing, Environ. Pollut. 145 (2) (2007) 571–576, https://doi.org/10.1016/j.envpol.2006.04.024.
[23] A.K. Sood, M. Aggarwal, J. Chem. Sci. 130 (2018) 39, https://doi.org/10.1007/s12039-018-1446-z.
[24] E. Lippmaa, M. Maegi, A. Samoson, M. Tarmak, G. Engelhardt, J. Am. Chem. Soc. 103 (17) (1981) 4992–4996, https://doi.org/10.1021/ja00407a002.
[25] A. Bolshakov, R. van de Poll, T. van Bergen-Brenkman, S.C.C. Wiedemann, N. Kosinov, E.J.M. Hensen, Appl. Catal. B Environ. 263 (2020) 118356, https://doi.org/10.1016/j.apcatb.2019.118356.
[26] M. Gackowski, J. Podobinski, E. Broclawik, J. Datka, Molecules 25 (2020) 31, https://doi.org/10.3390/molecules25010031.

[27] J. van Aelst, M. Haouas, E. Gobechiya, K. Houthoofd, A. Philippaerts, S.P. Sree, C. E.A. Kirschhock, P. Jacobs, J.A. Martens, B.F. Sels, F. Taulelle, J. Phys. Chem. C 118 (2014) 22573–22582, https://doi.org/10.1021/jp5107982.
[28] K. Chen, Z. Gan, S. Horstmeier, J.L. White, J. Am. Chem. Soc. 143 (2021) 6669–6680, https://doi.org/10.1021/jacs.1c02361.
[29] J.C. Groen, L.A.A. Peffer, J. Pérez-Ramírez, Microporous Mesoporous Mater. 60 (2003) 1–17, https://doi.org/10.1016/S1387-1811(03)00339-1.
[30] M. Thommes, K. Kaneko, A.V. Neimark, J.P. Olivier, F. Rodríguez-Reinoso, J. Rouquerol, K.S.W. Sing, Appl. Chem. 87 (9–10) (2015) 1051–1069, https://doi.org/10.1515/pac-2014-1117.
[31] D.C.H. Cheng, E. Gulari, J. Colloid Interface Sci. 90 (2) (1982) 410–423, https://doi.org/10.1016/0021-9797(82)90308-3.
[32] C. Direksilp, A. Sirivat, Polymers 12 (2020) 1023, https://doi.org/10.3390/polym12051023.
[33] T. Yokoi, Sci. Instrument News 7 (2016) 17–23.
[34] J. Chen, X. Lu, J. Mater. Cycles Waste Manag. 20 (2018) 489–495, https://doi.org/10.1007/s10163-017-0605-5.